



Cite this: DOI: 10.1039/c5dt03514g

Explaining the mechanical mechanisms of zeolitic metal–organic frameworks: revealing auxeticity and anomalous elasticity

Matthew. R. Ryder and Jin-Chong Tan*

The comprehensive elastic properties of Zeolitic Imidazolate Frameworks (ZIF-1 to ZIF-4) have been computed using density functional theory (DFT). We employed the periodic CRYSTAL14 code to calculate the single-crystal elastic coefficients (C_{ij}) at the B3LYP level of theory. While the chemical compositions of ZIFs-1 to -4 are the same, each structure features a distinct network topology, crystal symmetry and porosity configuration, which translate into differential structure-function mechanical correlations. We elucidate the anisotropic mechanical response with respect to the directionally dependent Young's and shear moduli properties. Our theoretical results suggest that ZIF-3 adopting a **dft** topology has an extremely low shear resistance ($G_{\min} = 0.1$ GPa), which is also underpinning the flexible mechanism responsible for its negative Poisson's ratio (auxetic $\nu_{\min} = -0.43$). Interestingly, we identified that ZIF-1, ZIF-2, and ZIF-4 could exhibit a nearly zero Poisson's ratio for certain crystal orientations, which is reminiscent of a rare "cork-like" phenomenon where there is practically no lateral deformation corresponding to an applied axial strain. Furthermore, we determined the bulk moduli and linear compressibilities, alongside the averaged elastic properties of the ZIF polycrystals.

Received 8th September 2015,
Accepted 22nd September 2015

DOI: 10.1039/c5dt03514g

www.rsc.org/dalton

1. Introduction

Understanding the mechanical properties and long-term durability of Metal–Organic Frameworks (MOFs) is considered as amongst the key challenges¹ to be addressed to guarantee the future success of this vibrant field. Whilst the chemical affinity and structural versatility of MOFs have been systematically studied and extensively characterised,² hitherto considerably little attention has been paid to its physical properties that are centrally important to many real-world applications.³ In principle, to be able to predict whether a MOF will remain structurally stable when subject to an external stress or pressure (*i.e.* not deforming excessively or collapsing under load), certain elementary data about its mechanical behaviour will be required (*e.g.* elasticity limit, plasticity response, fatigue and fracture).⁴ However, such detailed mechanical information associated with MOFs remains scarce.⁵

Foregoing notwithstanding, it is comforting to see that there has been an increasing range of research activities evolving in the past five years devoted to the emerging area which we termed "MOF mechanics", encompassing

both theoretical and experimental studies as exemplified below:

(A) Application of first-principles computational methods to derive the theoretical values of single-crystal elastic constants, from which the elastic anisotropy and network flexibility can be characterised.^{6–10} Albeit far fewer studies have considered the influence of crystal defects or large-strain (plastic) deformation on MOF mechanics.¹¹

(B) Experimental studies to ascertain the bulk modulus and linear compressibility of MOFs using diamond anvil cells;^{12,13} hardness and Young's modulus measurements by means of nanoindentation;^{14,15} shear modulus measurement using laser Brillouin scattering;⁷ and nanoscratch experiments to characterise the cohesion and interfacial adhesion strengths of polycrystalline MOF films.¹⁶ There are also studies exploring the tribological behaviours of MOF nanoparticles¹⁷ as well as that of polymer-MOF mixed-matrix membranes.¹⁸

(C) Combined experimental and theoretical methodologies to establish the Terahertz dynamics and collective lattice vibrations of MOFs employing high-resolution spectroscopic techniques.^{19,20} This latest direction of study could offer rich insights into the basis of framework flexibility and to pinpointing potential sources of structural destabilisation. It enables detailed elucidation of reversible gate-opening dynamics, and for probing host–guest confinement and temperature effects have on MOF mechanics.

Department of Engineering Science, University of Oxford, Parks Road, Oxford OX1 3PJ, UK. E-mail: jin-chong.tan@eng.ox.ac.uk

From the materials science and engineering perspective, MOF robustness in a manufacturing setting is a major challenge yet to be addressed.¹ Mechanical resilience⁴ is essential to afford high-throughput commercial shaping processes using conventional or emergent manufacturing technologies, such as extrusion, spray deposition, ball milling and powder palletising, 3-D printing and laser sintering, electrospinning of textiles *etc.* There is scope to advance the aforementioned manufacturing areas if the basic mechanical and physical properties information of MOFs is made available to engineers and technologists. Moreover, elucidating how the mechanics of MOFs can be tuned *via* chemical transformations,²¹ or by exploiting the mechanism of thermo-mechanical destabilisation^{22,23} could yield new multifunctional applications whereby an amorphous MOF phase can be used for encapsulating drug molecules,²⁴ luminescent guests, and toxic substances alike.²⁵

From a more fundamental point of view, basic research on MOF mechanics can open the door to the discovery of exotic mechanical characteristics, for example zero Poisson's ratio (ZPR),²⁶ negative Poisson's ratio (auxeticity or NPR),²⁷ negative linear compressibility (NLC)¹² and negative thermal expansion (NTE), all of which controlled by the detailed chemical bonding and coordination framework architecture underpinning modular MOF structures. These so-called "mechanical metamaterials"²⁸ are extremely attractive for example to engineer crack-resistant thin-film devices and multifunctional coatings; provided that the aforementioned manufacturing challenges can be alleviated. Above all, the basic science of MOF mechanics focusing on detailed elasticity analysis provides the crucial incipient point to comprehending many associated MOF mechanical behaviours beyond the elastic limit, which include but not limited to structural yielding and irreversible plastic deformation,²⁹ cracking and intermolecular rupture,³⁰ and MOF structural distortions triggered by elastic destabilisation, amorphisation³¹ and mechanochemistry.²³

In this work, we set out to explore the mechanical bounds of Zeolitic Imidazolate Frameworks (ZIFs),³² which represent an important subfamily of MOFs with potential for technological applications. In particular, herein we focus on the elastic properties of four ZIF structures, ZIFs-1 to -4, all of which featuring an identical chemical composition $\text{Zn}(\text{Im})_2$ where its divalent Zn^{2+} cations are coordinated to unsubstituted imidazolate linkers [$\text{Im} = \text{C}_3\text{H}_3\text{N}_2^-$]. However, their crystal symmetries, network topologies, geometrical parameters and physical properties are remarkably different. Using *ab initio* theoretical calculations, we demonstrate that the elastic characteristics and structure-property relationships of ZIF-1 to ZIF-4 are distinctive to each framework. We have uncovered a number of previously unreported elastic anomalies of ZIFs, for which we have identified the molecular origins and their physical significance.

2. Computational methodology

The *ab initio* calculations were performed using density functional theory (DFT), implemented by the periodic code,

CRYSTAL14.³³ The code uses Gaussian-type atom-centred all-electron basis sets. More specifically, 2032 basis functions were used for ZIF-1 and 4064 basis functions were used for ZIF-2, ZIF-3 and ZIF-4 (due to ZIF-1 having 136 atoms in the unit cell and the other three having 272). The geometries of each material were optimised at the B3LYP level of theory by relaxation of both the lattice parameters and atomic coordinates. To ensure the optimised structures were accurate we increased the convergence criteria of the route mean square (RMS) of the gradient and the displacement, from the default values of 0.0003 a.u. and 0.0012 a.u. to 0.0002 a.u. and 0.0004 a.u. respectively. In addition, we also tightened the self-consistent field (SCF) convergence threshold on the total energy from 10^{-7} a.u. to 10^{-8} a.u. and implemented tighter tolerances for the evaluation of two-electron integrals. The single-crystal elastic constants, C_{ij} , of the elasticity matrix (tensor) were then computed by using the numerical first derivative of the analytic cell gradients,³³ which corresponds to the individual elastic stiffness coefficients C_{ij} . The coefficients were obtained from deforming the optimised structure using a three-point formula in the symmetrically required directions of both positive and negative amplitudes, corresponding to tensile and compressive strains respectively. The magnitude of the strain along each given deformation is defined as 1%, to remain in the purely elastic response region. The mechanical properties were calculated *via* tensorial analysis implemented in Mathematica and the ELAM code.³⁴ The solvent accessible volumes (SAV) were calculated using the PLATON code.³⁵

3. Results and discussion

3.1. Crystal structures and porous ZIF network topologies

The four ZIF materials discussed in this work all have the same identical chemical composition $\text{Zn}(\text{Im})_2$, due to them all being Zn-based and possessing the unsubstituted imidazole linker ($\text{Im} = \text{C}_3\text{H}_3\text{N}_2^-$). All the structures feature the Zn-Im-Zn connectivity. Although each of the materials has the same chemical basis, they are all unique structures as shown in Fig. 1, and their structural and physical parameters are summarised in Table 1. ZIF-1 and ZIF-2 share the same network topology, that of **crb**, whereas ZIF-3 and ZIF-4 have the **dft** and **cag** network topologies, respectively. However, the network topologies are only an indication of the connectivity of the various atoms and do not necessarily mean that the response of the frameworks will be correlated. This is confirmed when we see that ZIF-2 and ZIF-4 have the same crystal symmetry (orthorhombic) despite having different topologies. What is possibly of more interest in the unique packing of each framework, as this has a direct effect on the porosity of the framework. The porosity can be described by multiple values but one of the most helpful is that of the solvent accessible volume (SAV),³⁵ as this can be a useful metric for applications such as gas storage or guest encapsulation. All of the structures considered in this work show large solvent accessible volumes; the largest being ZIF-3, closely followed by ZIF-2, with almost 60%

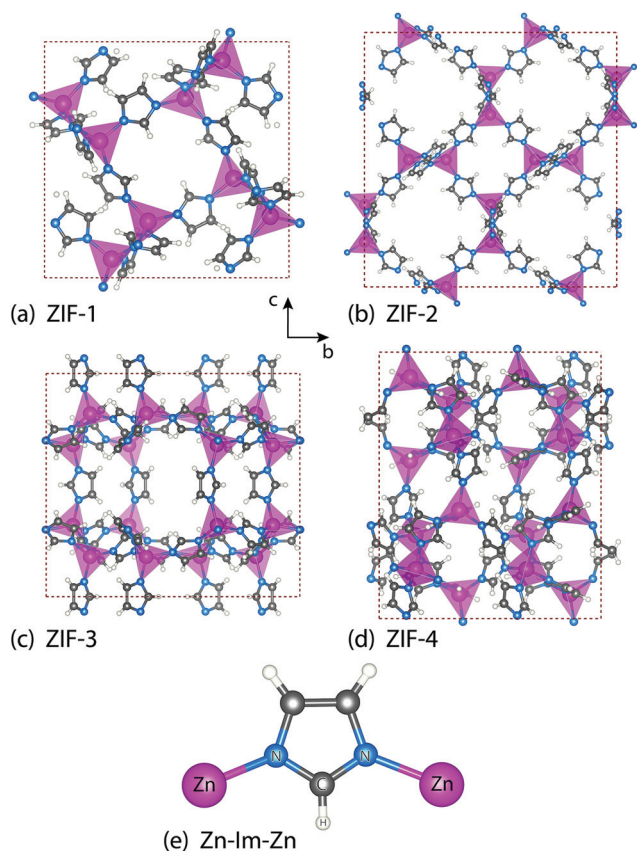


Fig. 1 Crystal structures of (a) ZIF-1, (b) ZIF-2, (c) ZIF-3, and (d) ZIF-4. (e) Zn–Im–Zn linkages subtending an angle of $\sim 145^\circ$ at the centre of the imidazolate ring. Purple tetrahedron is ZnN_4 . Colour code used: zinc purple; carbon grey; nitrogen blue; hydrogen white.

Table 1 Structural properties of ZIF-1 to ZIF-4

ZIF- <i>n</i>	Symmetry	Density	SAV	Topology	<i>T/V</i>
ZIF-1	Monoclinic	1.101	33.9	crb	3.64
ZIF-2	Orthorhombic	0.932	56.1	crb	2.80
ZIF-3	Tetragonal	0.803	57.7	dft	2.66
ZIF-4	Orthorhombic	1.032	34.3	cag	3.68

Density = g cm^{-3} ; T/V = density of metal atoms per nm^3 ; 32 SAV = solvent accessible volume (%).

Table 2 Single-crystal elastic stiffness coefficients (C_{ij}) of ZIF-1 to ZIF-4

ZIF- <i>n</i>	C_{11}	C_{22}	C_{33}	C_{44}	C_{55}	C_{66}	C_{12}	C_{13}	C_{15}	C_{23}	C_{25}	C_{35}	C_{46}
ZIF-1	8.337	4.115	4.585	1.700	1.565	1.198	1.893	2.297	−0.853	1.250	−0.495	−0.866	0.044
ZIF-2	7.688	8.218	4.890	1.266	1.540	1.114	5.413	3.418	—	4.457	—	—	—
ZIF-3	3.803	$=C_{11}$	6.197	0.857	$=C_{44}$	1.528	3.581	3.520	—	$=C_{13}$	—	—	—
ZIF-4 ^a	3.073	3.361	2.953	0.771	0.903	1.532	0.574	0.603	—	0.770	—	—	—

^a Revised CRYSTAL DFT calculations adopting a higher level of theory (B3LYP), compared with a recent theoretical study (PBE).¹⁰

of the internal volume being accessible to solvent (probe size 1.2 Å). This characteristic appears to be logically linked to the packing of the frameworks and a good measure of this is the number of metal centres (*i.e.* ZnN_4 tetrahedral sites)¹⁴ present in each unit cell, designated as T/V . It is therefore not surprising that ZIF-2 and ZIF-3 have the fewest number of Zn atoms per unit cell compared to the other two structures and, this is also represented by the physical densities of each ZIF material.

3.2. Single-crystal elastic stiffness coefficients C_{ij}

The mechanical properties discussed in our work were calculated by tensorial analysis of the single-crystal elastic constants, C_{ij} . This is due to Hooke's law being related to stress σ and strain ϵ (both second-rank tensors) in the following equation:

$$\sigma_{ij} = \sum_{kl} C_{ijkl} \epsilon_{kl}$$

where C_{ijkl} represents the symmetric fourth-rank elasticity tensor³⁶ that has up to 21 unique (independent) elastic constants, depending on the symmetry of the system. We note that ZIF-1 has thirteen elastic constants due to being monoclinic, whereas ZIF-2 and ZIF-4 have nine and ZIF-3 has six due to being orthorhombic and tetragonal, respectively. All of the computed single-crystal elastic constants are summarised for each system in Table 2. The symmetric elasticity matrix, also called the stiffness tensor has the following form:

$$C_{\text{monoclinic}} = \begin{pmatrix} C_{11} & C_{12} & C_{13} & 0 & C_{15} & 0 \\ & C_{22} & C_{23} & 0 & C_{25} & 0 \\ & & & C_{33} & 0 & C_{35} \\ & & & & C_{44} & 0 \\ & & & & & C_{55} \\ \text{symm.} & & & & & & C_{66} \end{pmatrix}$$

The diagonal coefficients C_{11} , C_{22} and C_{33} represent the stiffness along each of the three principal crystal axes, a , b , and c under a uniaxial strain. The other diagonal coefficients C_{44} , C_{55} and C_{66} are the stiffness against angular distortions when subjected to shear strains. The off-diagonal coefficients correspond to coupling effects, tensile–tensile coupling (*e.g.* C_{12} , C_{13} and C_{23}) between any two orthonormal axes and are present for all four structures, but the C_{i5} coefficients ($i = 1, 2, 3$) are only present for ZIF-1 due to the monoclinic symmetry and

represent tensile–shear coupling, finally the C_{46} coefficient represents shear–shear coupling. These are only present for ZIF-1 due to $\beta \neq 90^\circ$. The mechanical properties are calculated from the inversion of the elasticity matrix (tensor), known as the compliance matrix in accordance to:

$$S_{ijkl} = C_{ijkl}^{-1}$$

3.3. Anisotropic framework stiffness subject to uniaxial tensile or compressive deformation (Young's modulus E)

The directional Young's modulus is defined as the ratio of uniaxial stress over uniaxial strain along a unit vector \mathbf{u} and can be seen in Fig. 2, where the surface corresponds to a spherical plot of $E(\mathbf{u})$ obtained from the following tensorial equation:

$$E(\mathbf{u}) = \frac{1}{u_i u_j u_k u_l S_{ijkl}}$$

The maximum values for the Young's moduli (E_{\max} in Table 3) are due to the direction of the compression (likewise tension) coinciding with the planarity of an aromatic ring of the imidazolate groups. This explains why the shapes of the 3-D surfaces are similar for ZIF-2 and ZIF-4, as the directions of the orientations of the aromatic rings are quite varied, however in the case of ZIF-4 the rings are less inclined in the

$\langle 001 \rangle$ axes thereby giving a more anisotropic appearance. An interesting feature is the maximum Young's modulus of ZIF-1 which is simply due to two aromatic rings being compressed per unit cell in the $\langle 100 \rangle$ direction, explaining why the Young's modulus ($E_{\max} = 6.88$ GPa) is almost a factor of two times greater than that of the other three structures (3.21–3.62 GPa) when there is only one aromatic ring in plane.

Lastly, the other interesting property is the minimum Young's modulus of ZIF-3, which is significantly lower than the other three structures, which all have much the same value. This is due to the deformation of the rings made up of the ZnN_4 tetrahedra; more specifically the most flexible 6-membered rings (6MR) present in ZIF-1, ZIF-2 and ZIF-4 (in this work) and ZIF-8 (in previous work)⁷ which give minimum Young's modulus values of 2.17–2.76 GPa. However, in ZIF-3 there is an even more flexible 8-membered ring (8MR) not present in the other ZIFs studied, and this results in an exceptionally low Young's modulus (E_{\min}) of just 0.42 GPa.

3.4. Exceedingly low framework rigidity under angular deformation (shear modulus G)

The shear modulus (or rigidity modulus) can also be shown as a 3-D representation, but depending on an additional unit vector \mathbf{v} , which is perpendicular to vector \mathbf{u} . The surfaces of the spherical plots in Fig. 3 are the maxima and minima of $G(\mathbf{u}, \mathbf{v})$ obtained from the following equation:

$$G(\mathbf{u}, \mathbf{v}) = \frac{1}{u_i v_j u_k v_l S_{ijkl}}$$

The maximum values are similar for each of the four structures (see G_{\max} in Table 3), with ZIF-1 being slightly higher due to the denser packing of the framework. The most interesting feature, however, is the significantly low minimum shear modulus of ZIF-3 with a $G_{\min} = 0.11$ GPa. It is predicted to be almost a factor of ten times lower than that of ZIF-8 ($G_{\min} \sim 1$ GPa), which was previously reported to be 'exceptionally low'.⁷ Therefore ZIF-3 has the lowest shear modulus ever predicted for a ZIF material. This results in ZIF-3 being considerably more anisotropic than the other frameworks discussed, and this is clearly demonstrated in the shape of the 3-D surface shown in Fig. 3. We postulated that this is likely the reason that ZIF-3 is limited to the powder form³⁷ because its structural shear instability (facile plane slippage)³⁸ may hinder the growth of sizeable crystals. Unfortunately, this effect has restricted any experiments investigating the elastic response of ZIF-3, such as Brillouin scattering or single-crystal nanoindentation work.

The reason that ZIF-3 is significantly less stable to shear strain is linked to the discussion about the uniaxial compression presented in section 3.3. The 8MR highlighted in Fig. 2 simply does not provide the same support as the 6MRs present in the other frameworks. In fact, this is not surprising as it is analogous to the difference in stability of cyclohexane (or benzene; in ZIF-8 due to the planarity of the 6MR)¹⁹ and cyclooctatetraene, due to the tetrahedral environment of the

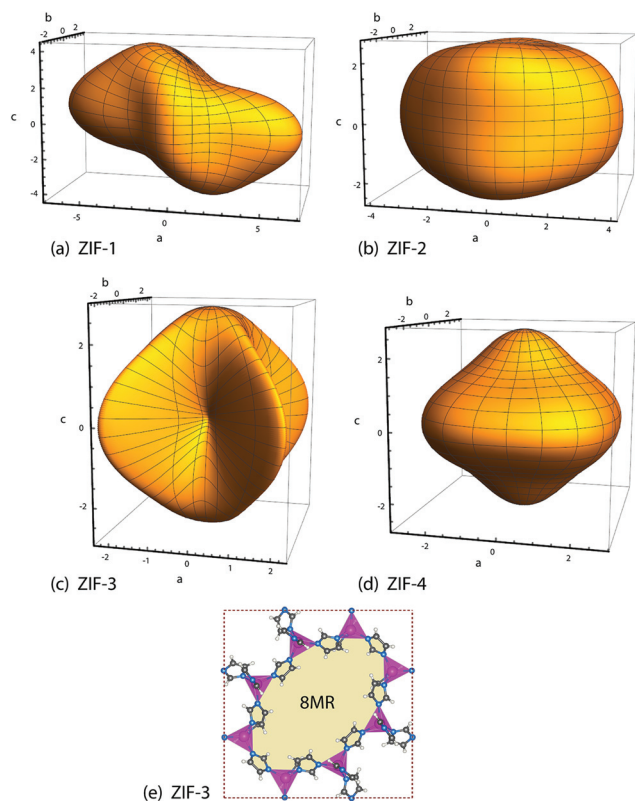


Fig. 2 Young's modulus representation surfaces $E(\mathbf{u})$ of (a) ZIF-1, (b) ZIF-2, (c) ZIF-3, and (d) ZIF-4. (e) Projection down the c -axis highlighting the location of an eight-membered ring (8MR) in ZIF-3.

Table 3 Mechanical properties of ZIF-1 to ZIF-4

Elastic property		ZIF-1	ZIF-2	ZIF-3	ZIF-4
Young's modulus, E (GPa)	E_{\max}	6.88	3.62	3.21	3.27
	E_{\min}	2.76	2.42	0.42	2.17
	$A_E = E_{\max}/E_{\min}$	2.49	1.50	7.64	1.51
Shear modulus, G (GPa)	G_{\max}	1.96	1.54	1.53	1.53
	G_{\min}	1.19	0.90	0.11	0.77
	$A_G = G_{\max}/G_{\min}$	1.65	1.72	13.91	1.99
Linear compressibility, β (TPa $^{-1}$)	β_{\max}	225.1	172.9	127.6	241.2
	β_{\min}	−0.6	−13.3	16.4	202.1
Poisson's ratio, ν	ν_{\max}	0.63	0.56	1.34	0.41
	ν_{\min}	0.03	0.07	−0.43	0.06

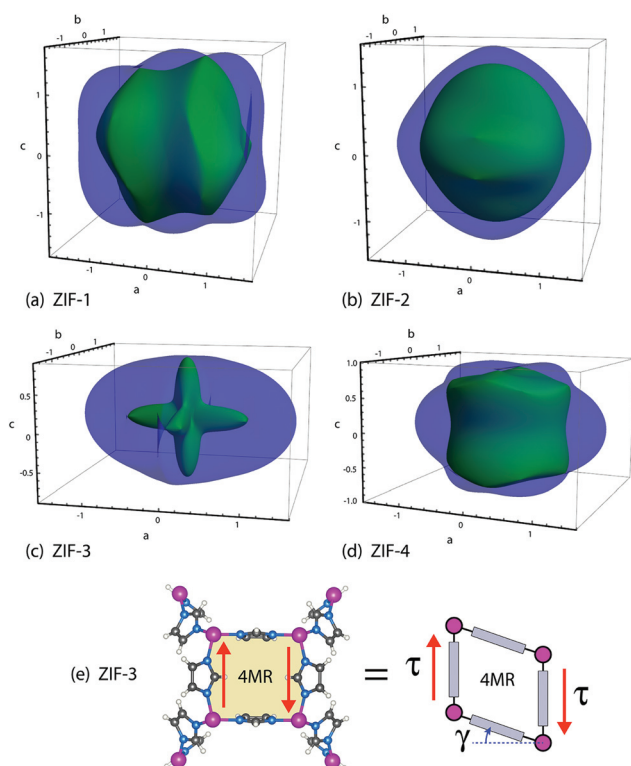


Fig. 3 Shear modulus representation surfaces $G(\mathbf{u}, \mathbf{v})$ of (a) ZIF-1, (b) ZIF-2, (c) ZIF-3, and (d) ZIF-4. The maximum and minimum values are represented as blue and green surfaces, respectively. (e) Projection down the [110] axis of ZIF-3, highlighting the location of the four-membered ring (4MR). The accompanying ‘pivot-and-strut’ model further emphasises its pliant 4-node configuration, which is highly susceptible to a shear strain γ (angular distortion) generated by a pair of antiparallel shear stresses τ .

Zn atoms and the linker imidazole groups sometimes mimicking alkene moieties, instead of alkane, due to the specific framework packing. There is therefore less structural hindrance in ZIF-3, which results in a decreased energy requirement for deformation and the mechanism responsible for the remarkably low shear modulus of 0.11 GPa is illustrated in Fig. 3. It is evident that there is negligible structural support restricting the shearing of the flexible 4MR (Fig. 3e) facilitated by the ‘boat’ conformation of the adjoining 8MRs (Fig. 2e).

A previous study showed that ZIF-1, ZIF-3 and ZIF-4 can all mechanically and thermally amorphise, albeit amorphisation by ball milling is considerably faster compared with heating (~ 300 °C) or under hydrostatic pressure.³⁷ Our new findings would reinforce the suggestion that the relatively low shear moduli of ZIFs (Table 3: $G_{\max} < 2$ GPa) is the cause of the ball-milling amorphisation and more generally shear-induced structural instability and collapse.¹⁹

3.5. Anomalous Poisson's ratio (ν) and auxeticity

The Poisson's ratio (ν) is analogous to the shear modulus in that it is also a function of two unit vectors. For this reason the 3-D surfaces shown in Fig. 4 are again the maxima and minima, however this time the minima is represented as green and red, for positive and negative values respectively. The Poisson's ratio represents the ratio of the transverse strain to the axial strain under uniaxial deformation and can be obtained from the following equation:

$$\nu(\mathbf{u}, \mathbf{v}) = -\frac{u_i u_j v_k v_l S_{ijkl}}{u_i u_j u_k u_l S_{ijkl}}$$

As mentioned in the introduction, negative Poisson's ratios (NPR) and zero Poisson's ratio (ZPR), are of great interest due to their possible applications. Firstly, it is worth mentioning that ZIF-8 was previously reported⁷ to have a minimum Poisson's ratio of 0.33 and this is due to the contrasting planarity of the 6MR compared to ZIF-1, ZIF-2 and ZIF-4. As mentioned in section 3.4, relating to the rigidity under angular deformation, the 6MR in ZIF-8 is planar (analogous to benzene) whereas the 6MRs in ZIF-1, ZIF-2 and ZIF-4 (which have a minimum Poisson's ratio approximately zero) are not (they are analogous to cyclohexane). This is the reason for the exciting ‘cork-like’ behaviour ($\nu \approx 0$),²⁷ as the deformation of the 6MR is akin to a cyclohexane ring inversion and as a result has negligible lateral dimension change upon axial strain in specific directions. This is observed clearly in the minimum 3-D surfaces, where a similar response is observed at rotated orientations, consistent with the coordination of the 6MRs.

However, of even greater interest is the significant negative Poisson's ratio predicted for ZIF-3 ($\nu_{\min} = -0.43$, see Table 3). This is again due to the unique presence of the 8MRs, which

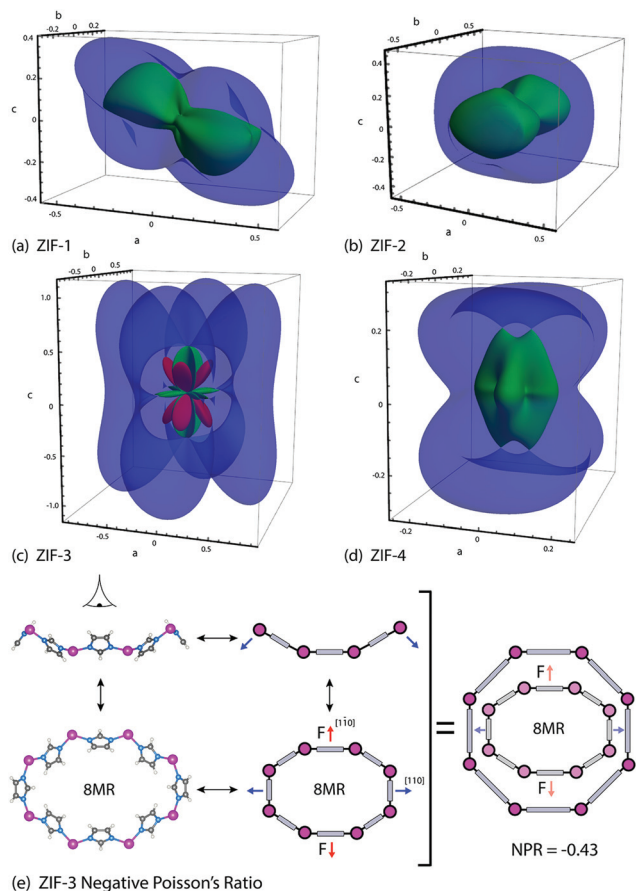


Fig. 4 Poisson's ratio representation surfaces $\nu(u,v)$ of (a) ZIF-1, (b) ZIF-2, (c) ZIF-3, and (d) ZIF-4. The maximum values are designated in blue, while green and red surfaces correspond to positive and negative minima, respectively. (e) View down the $[1\bar{1}0]$ and $[001]$ axes of ZIF-3, showing the 'boat-like' conformation of the eight-membered ring (8MR). The diagram to the right demonstrates the mechanism involved when force is applied in the $[1\bar{1}0]$ direction, depicting both (an amplified) lateral and transverse extension of the 8MR explaining the anomalous auxetic response.

are distinct from the 'chair' conformations of the 6MRs in ZIF-1, ZIF-2 and ZIF-4, and the planar 6MRs in ZIF-8. The 8MRs in ZIF-3 display a 'boat-like' conformation analogous to that of cyclooctatetraene and can be seen in Fig. 4. This 'boat' conformation is hence the reason for the extraordinary response to deformation. It occurs due to the elongation in the loading axis propagating an elongation in the transverse direction as well instead of a contraction, due to the ring expansion upon planarity. ZIF-3 is so far the only ZIF structure possessing an 8MR to have its mechanical properties investigated and highlights the interesting phenomenon that are possibly still undiscovered for ZIFs.

3.6. Negative linear compressibility (NLC)

The anisotropic linear compressibility $\beta(\mathbf{u})$ represents the compression along an axis upon isostatic compression and can be

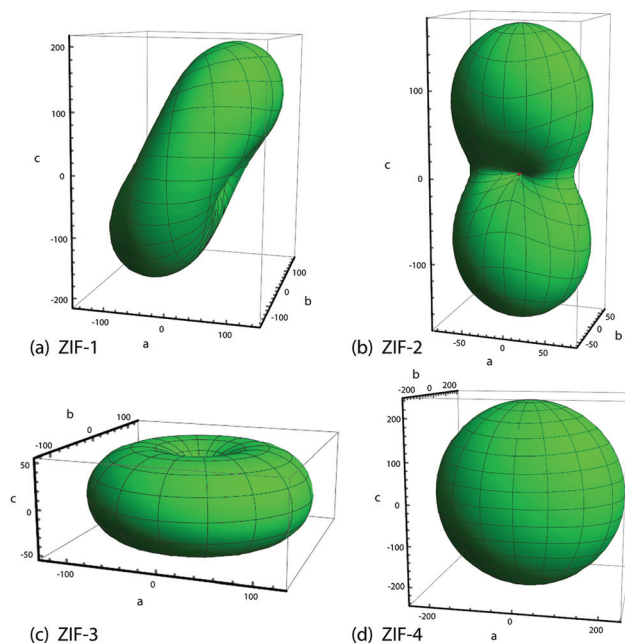


Fig. 5 Linear compressibility representation surfaces $\beta(\mathbf{u})$ of (a) ZIF-1, (b) ZIF-2, (c) ZIF-3, and (d) ZIF-4. The green and red surfaces (the latter is relatively small in ZIFs-1 and -2) designate positive and negative compressibility, respectively.

obtained from the following equation:

$$\beta(\mathbf{u}) = u_i u_j S_{ijkl}$$

The 3-D anisotropic surfaces are shown in Fig. 5, with the positive and negative values shown as green and red respectively. It is worth noting that the magnitude of the negative linear compressibility (NLC) present in ZIF-1 and ZIF-2 are considerably lower than their respective maxima. The NLC values for ZIF-1 and ZIF-2 are small and are likely due to the linkers rotating slightly upon compression. The increased maximum values for ZIF-1 and ZIF-4 compared to ZIF-2 and ZIF-3 is due to the presence of pore channels in the latter. ZIF-3 has its minima in the direction of the pore channel and shows a transverse isotropic response due to its tetragonal symmetry. ZIF-4 shows an almost isotropic response due to the uniformity of the pores in each direction, unlike the other three frameworks.

3.7. Hydrostatic response under uniform compression loading

The bulk modulus of a material is its resistance to (uniform) hydrostatic compression and the values given in this work (Table 4) are the Voigt–Reuss–Hill (VRH) averages. The Voigt values assume a uniform strain, the Reuss values correspond to a uniform stress, and the Voigt–Reuss–Hill values are the average of the two.³⁶ All of the four materials give values in the range of 1.5–5.0 GPa, confirming that ZIF structures are in general more compressible when compared to other MOFs, such as HKUST-1 (~25 GPa),⁶ UiOs (14–42 GPa),⁹ and MILs (1–20 GPa).⁸ There is, however, no obvious correlation with the

Table 4 Isotropic aggregate elastic properties based on the Voigt–Reuss–Hill (VRH) averages, corresponding to a texture-free polycrystalline material. The bulk (K), Young's (E) and shear (G) moduli are in GPa. Poisson's ratio (ν) is dimensionless

ZIF- n	K_{VRH}	E_{VRH}	G_{VRH}	ν_{VRH}
ZIF-1	2.76	4.00	1.59	0.26
ZIF-2	4.88	3.44	1.25	0.38
ZIF-3	3.79	1.77	0.62	0.42
ZIF-4	1.54	2.69	1.11	0.21

densities or packing of the frameworks due to all four structures having significantly large solvent accessible volumes (Table 1). It is worth noting that the calculated values are based on perfect polycrystalline materials assuming no residual solvent molecules or defects. It is therefore safe to assume that the experimental values that could be obtained would be relatively higher.

3.8. Polycrystalline powder averaged mechanical properties

In the context of novel materials manufacturing and commercial product designs, bulk properties of an isotropic material are key data for conducting engineering-based stress–strain calculations. Table 4 summarises the isotropic averaged properties of E , G and ν , which physically correspond to a homogeneous powder compact fabricated by a palletisation process. These values can also be used to approximate the elastic properties of ZIF thin-film coatings and bulk extrudates provided that their polycrystalline grain arrangements are in fact randomly oriented (*i.e.* no preferred textures). Notably, our data in Table 4 reveal that the shear moduli of the aggregate is relatively small where the upper and lower bounds respectively are 1.6 GPa and 0.6 GPa, substantiating the hypothesis that mechanical amorphisation of polycrystalline ZIF powders³⁷ could be straightforwardly triggered by shear-induced angular distortions causing an eventual framework collapse.⁷ It is important to note that the aggregate Poisson's ratio of ZIF-3 is determined to be positive ($\nu_{\text{VRH}} = 0.42$) despite exhibiting a relatively strong auxetic response ($\nu_{\text{min}} = -0.43$) in single crystal form. This result highlights the non-trivial challenge to developing a controlled growth methodology for manufacturing polycrystalline MOF films, which accurately matches the crystallographic orientations predicted for maximum auxeticity if such an effect is to be practically useful.

4. Conclusions

By means of *ab initio* density functional theory (DFT), we have computed and assessed the complete elastic properties of four structurally polymorphic ZIFs. The structures of ZIFs-1 to -4 are constructed from divalent Zn(II) cations coordinated by unsubstituted imidazolate linkers, conferring very distinctive network topologies, porosity, and physical properties. Notably, our calculations indicated that ZIF-1, ZIF-2, ZIF-3 and

ZIF-4 may exhibit interesting mechanical behaviours, ranging from an almost zero Poisson's ratio to auxeticity (NPR), and from negative linear compressibility to an extremely low shear modulus in ZIF-3. Our theoretical approach provides new insights into the molecular mechanisms surrounding their elastic anisotropy, thereby enabling us to elucidate the anomalous elastic phenomena highlighted above. Overall, our findings reiterate the many undiscovered possibilities offered by the field of MOF mechanics, and the exciting opportunities that it might bring to basic science (mechanical metamaterials) and practical engineering. It is our hope that the detailed mechanical data and new property predictions discussed herein will be advantageous to guide the future experimentation, design and manufacturing, and follow-on theoretical work of ZIFs and flexible MOF materials.

Acknowledgements

M. R. R. thanks the UK Engineering and Physical Sciences Research Council (EPSRC) for the DTA postgraduate scholarship and an additional scholarship from the Science and Technology Facilities Council (STFC) CMSD Award 13-05. The authors would like to acknowledge the use of the University of Oxford Advanced Research Computing (ARC) facility in carrying out this work (<http://dx.doi.org/10.5281/zenodo.22558>). We are grateful to the SCARF cluster at the Rutherford Appleton Laboratory for provision of additional computing resources.

References

- 1 M. D. Allendorf and V. Stavila, *CrystEngComm*, 2015, **17**, 229–246.
- 2 H. C. Zhou, J. R. Long and O. M. Yaghi, *Chem. Rev.*, 2012, **112**, 673–674; H. Furukawa, K. E. Cordova, M. O'Keeffe and O. M. Yaghi, *Science*, 2013, **341**, 974–986.
- 3 A. G. Slater and A. I. Cooper, *Science*, 2015, **348**, aaa8075; M. R. Ryder and J. C. Tan, *Mater. Sci. Technol.*, 2014, **30**, 1598–1612; P. Silva, S. M. F. Vilela, J. P. C. Tomé and F. A. Almeida Paz, *Chem. Soc. Rev.*, 2015, **44**, 6774–6803.
- 4 J. C. Tan and A. K. Cheetham, *Chem. Soc. Rev.*, 2011, **40**, 1059–1080.
- 5 W. Li, S. Henke and A. K. Cheetham, *APL Mater.*, 2014, **2**, 123902.
- 6 M. Tafipolsky, S. Amirjalayer and R. Schmid, *J. Phys. Chem. C*, 2010, **114**, 14402–14409.
- 7 J. C. Tan, B. Civalleri, C. C. Lin, L. Valenzano, R. Galvelis, P. F. Chen, T. D. Bennett, C. Mellot-Draznieks, C. M. Zicovich-Wilson and A. K. Cheetham, *Phys. Rev. Lett.*, 2012, **108**, 095502.
- 8 A. U. Ortiz, A. Boutin, A. H. Fuchs and F.-X. Coudert, *Phys. Rev. Lett.*, 2012, 109.
- 9 H. Wu, T. Yildirim and W. Zhou, *J. Phys. Chem. Lett.*, 2013, **4**, 925–930.

- 10 J. C. Tan, B. Civalleri, A. Erba and E. Albanese, *CrystEngComm*, 2015, **17**, 375–382.
- 11 V. Ishwar Hegde, J.-C. Tan, U. V. Waghmare and A. K. Cheetham, *J. Phys. Chem. Lett.*, 2013, **4**, 3377–3381; A. U. Ortiz, A. Boutin, A. H. Fuchs and F.-X. Coudert, *J. Phys. Chem. Lett.*, 2013, **4**, 1861–1865.
- 12 W. Li, M. R. Probert, M. Kosa, T. D. Bennett, A. Thirumurugan, R. P. Burwood, M. Parinello, J. A. K. Howard and A. K. Cheetham, *J. Am. Chem. Soc.*, 2012, **134**, 11940–11943.
- 13 P. Serra-Crespo, A. Dikhtiarenko, E. Stavitski, J. Juan-Alcañiz, F. Kapteijn, F.-X. Coudert and J. Gascon, *CrystEngComm*, 2015, **17**, 276–280.
- 14 J. C. Tan, T. D. Bennett and A. K. Cheetham, *Proc. Natl. Acad. Sci. U. S. A.*, 2010, **107**, 9938–9943.
- 15 S. Bundschuh, O. Kraft, H. K. Arslan, H. Gliemann, P. G. Weidler and C. Wöll, *Appl. Phys. Lett.*, 2012, **101**, 101910; S. Henke, W. Li and A. K. Cheetham, *Chem. Sci.*, 2014, **5**, 2392–2397; T. D. Bennett, J. Sotelo, J. C. Tan and S. A. Moggach, *CrystEngComm*, 2015, **17**, 286–289.
- 16 B. Van de Voorde, R. Ameloot, I. Stassen, M. Everaert, D. De Vos and J. C. Tan, *J. Mater. Chem. B*, 2013, **1**, 7716–7724; I. Buchan, M. R. Ryder and J. C. Tan, *Cryst. Growth Des.*, 2015, **15**, 1991–1999; I. Stassen, M. Styles, T. Van Assche, N. Campagnol, J. Fransaer, J. Denayer, J. C. Tan, P. Falcaro, D. De Vos and R. Ameloot, *Chem. Mater.*, 2015, **27**, 1801–1807.
- 17 Q. Shi, Z. F. Chen, Z. W. Song, J. P. Li and J. X. Dong, *Angew. Chem., Int. Ed.*, 2011, **50**, 672–675.
- 18 N. W. Khun, E. M. Mahdi, S. Q. Ying, T. Sui, A. M. Korsunsky and J. C. Tan, *APL Mater.*, 2014, **2**, 124101.
- 19 M. R. Ryder, B. Civalleri, T. D. Bennett, S. Henke, S. Rudić, G. Cinque, F. Fernandez-Alonso and J. C. Tan, *Phys. Rev. Lett.*, 2014, **113**, 215502.
- 20 N. Tan, M. T. Ruggiero, C. Orellana-Tavra, T. Tian, A. D. Bond, T. M. Korter, D. Fairen-Jimenez and J. A. Zeitler, *Chem. Commun.*, 2015, DOI: 10.1039/C5CC06455D.
- 21 R. J. Marshall, S. L. Griffin, C. Wilson and R. S. Forgan, *J. Am. Chem. Soc.*, 2015, **137**, 9527–9530.
- 22 T. D. Bennett, J.-C. Tan, Y. Yue, E. Baxter, C. Ducati, N. J. Terrill, H. H. M. Yeung, Z. Zhou, W. Chen, S. Henke, A. K. Cheetham and G. N. Greaves, *Nat. Commun.*, 2015, **6**, 8079.
- 23 A. D. Katsenis, A. Puskaric, V. Strukil, C. Mottillo, P. A. Julien, K. Uzarevic, M. H. Pham, T. O. Do, S. A. Kimber, P. Lazic, O. Magdysyuk, R. E. Dinnebier, I. Halasz and T. Friscic, *Nat. Commun.*, 2015, **6**, 6662.
- 24 C. Orellana-Tavra, E. F. Baxter, T. Tian, T. D. Bennett, N. K. Slater, A. K. Cheetham and D. Fairen-Jimenez, *Chem. Commun.*, 2015, **51**, 13878–13881.
- 25 T. D. Bennett, P. J. Saines, D. A. Keen, J. C. Tan and A. K. Cheetham, *Chem. – Eur. J.*, 2013, **19**, 7049–7055.
- 26 Z. A. D. Lethbridge, R. I. Walton, A. S. H. Marmier, C. W. Smith and K. E. Evans, *Acta Mater.*, 2010, **58**, 6444–6451.
- 27 G. N. Greaves, A. L. Greer, R. S. Lakes and T. Rouxel, *Nat. Mater.*, 2011, **10**, 823–837.
- 28 R. Gatt, L. Mizzi, J. I. Azzopardi, K. M. Azzopardi, D. Attard, A. Casha, J. Briffa and J. N. Grima, *Sci. Rep.*, 2015, **5**, 8395.
- 29 J. C. Tan, P. J. Saines, E. G. Bithell and A. K. Cheetham, *ACS Nano*, 2012, **6**, 615–621.
- 30 J. C. Tan, C. A. Merrill, J. B. Orton and A. K. Cheetham, *Acta Mater.*, 2009, **57**, 3481–3496.
- 31 T. D. Bennett, A. L. Goodwin, M. T. Dove, D. A. Keen, M. G. Tucker, E. R. Barney, A. K. Soper, E. G. Bithell, J. C. Tan and A. K. Cheetham, *Phys. Rev. Lett.*, 2010, **104**, 115503.
- 32 A. Phan, C. J. Doonan, F. J. Uribe-Romo, C. B. Knobler, M. O’Keeffe and O. M. Yaghi, *Acc. Chem. Res.*, 2010, **43**, 58–67.
- 33 R. Dovesi, R. Orlando, A. Erba, C. M. Zicovich-Wilson, B. Civalleri, S. Casassa, L. Maschio, M. Ferrabone, M. De La Pierre, P. D’Arco, Y. Noël, M. Causà, M. Rérat and B. Kirtman, *Int. J. Quantum Chem.*, 2014, **114**, 1287–1317.
- 34 A. Marmier, Z. A. D. Lethbridge, R. I. Walton, C. W. Smith, S. C. Parker and K. E. Evans, *Comput. Phys. Commun.*, 2010, **181**, 2102–2115.
- 35 A. L. Spek, *J. Appl. Crystallogr.*, 2003, **36**, 7–13.
- 36 J. F. Nye, *Physical Properties of Crystals*, Clarendon Press, Oxford, 1957.
- 37 T. D. Bennett, S. Cao, J. C. Tan, D. A. Keen, E. G. Bithell, P. J. Beldon, T. Friscic and A. K. Cheetham, *J. Am. Chem. Soc.*, 2011, **133**, 14546–14549.
- 38 T. Beyer, G. M. Day and S. L. Price, *J. Am. Chem. Soc.*, 2001, **123**, 5086–5094.